Article

Cell Chemical Biology

Small Molecule Inhibition of CPS1 Activity through an Allosteric Pocket

Graphical Abstract

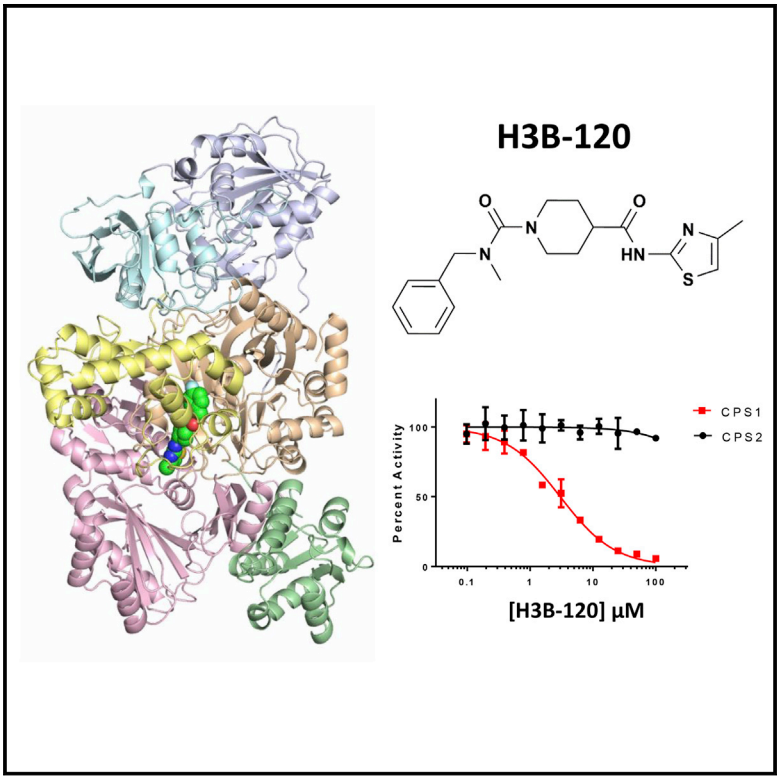

Authors

Shihua Yao, Tuong-Vi Nguyen, Alan Rolfe, ..., Ping Zhu, Nicholas A. Larsen, David M. Bolduc

Correspondence

david_bolduc@h3biomedicine.com

In Brief

CPS1 is a proposed oncoprotein of interest for drug development. Yao et al. describe the discovery of small-molecule inhibitors of CPS1 and discuss their proposed impact for studying CPS1 cancer biology.

Highlights

- A high-throughput screen identifies a small-molecule inhibitor of CPS1, H3B-120
- H3B-120 binds to an allosteric pocket to achieve highly selective inhibition of CPS1
- Analogs of H3B-120 block CPS1 cellular activity in primary human hepatocytes

Yao et al., 2020, Cell Chemical Biology *27*, 259–268
March 19, 2020
https://doi.org/10.1016/j.chembiol.2020.01.009

CellPress

Cell Chemical Biology
Article

Small Molecule Inhibition of CPS1 Activity through an Allosteric Pocket

Shihua Yao,[1,4] Tuong-Vi Nguyen,[1,4] Alan Rolfe,[1] Anant A. Agrawal,[1] Jiyuan Ke,[1] Shouyong Peng,[1] Federico Colombo,[1] Sean Yu,[2] Patricia Bouchard,[3] Jiayi Wu,[1] Kuan-Chun Huang,[1] Xingfeng Bao,[1] Kiyoyuki Omoto,[1] Anand Selvaraj,[1] Lihua Yu,[1] Stephanos Ioannidis,[1] Frédéric H. Vaillancourt,[1] Ping Zhu,[1] Nicholas A. Larsen,[1] and David M. Bolduc[1,5,*]
[1]H3 Biomedicine Inc., 300 Technology Square, Cambridge, MA 02139, USA
[2]RMI Laboratories LLC, 418 Industrial Drive, North Wales, PA 19454, USA
[3]NMX Research and Solutions, Inc., 500 Cartier Boulevard W., Laval, Quebec H7V 5B7, Canada
[4]These authors contributed equally
[5]Lead Contact
*Correspondence: david_bolduc@h3biomedicine.com
https://doi.org/10.1016/j.chembiol.2020.01.009

SUMMARY

Carbamoyl phosphate synthetase 1 (CPS1) catalyzes the first step in the ammonia-detoxifying urea cycle, converting ammonia to carbamoyl phosphate under physiologic conditions. In cancer, CPS1 overexpression supports pyrimidine synthesis to promote tumor growth in some cancer types, while in others CPS1 activity prevents the buildup of toxic levels of intratumoral ammonia to allow for sustained tumor growth. Targeted CPS1 inhibitors may, therefore, provide a therapeutic benefit for cancer patients with tumors overexpressing CPS1. Herein, we describe the discovery of small-molecule CPS1 inhibitors that bind to a previously unknown allosteric pocket to block ATP hydrolysis in the first step of carbamoyl phosphate synthesis. CPS1 inhibitors are active in cellular assays, blocking both urea synthesis and CPS1 support of the pyrimidine biosynthetic pathway, while having no activity against CPS2. These newly discovered CPS1 inhibitors are a first step toward providing researchers with valuable tools for probing CPS1 cancer biology.

INTRODUCTION

The primary function of the urea cycle under normal physiologic conditions is to remove toxic ammonia from the blood that is produced as a byproduct of amino acid catabolism (Adeva et al., 2012). In cancer, malignant cells have found ways to re-wire this metabolic pathway to support cell growth (Keshet et al., 2018). This is primarily achieved through two mechanisms: one, the differential expression of individual urea cycle genes to repurpose urea cycle metabolites for the support of anabolic pathways, especially pyrimidine synthesis. Two, upregulation of total urea cycle activity to prevent the accumulation of ammonia within tumors that in some cancer types may be toxic to cell growth. There are five enzymes in the urea cycle: carbamoyl phosphate synthetase 1 (CPS1), ornithine transcarbamylase (OTC), argininosuccinate synthase (ASS1), argininosuccinate lyase (ASL), and arginase (ARG) (Adeva et al., 2012). Several studies have demonstrated that reduced activity of OTC, ASS1, and ASL diverts urea cycle metabolites to the pyrimidine biosynthetic pathway in both cancer and urea cycle deficiency syndromes (Brosnan and Brosnan, 2007; Gerrits et al., 1993; van Kuilenburg et al., 2006; Lee et al., 2018; Rabinovich et al., 2015; Salerno et al., 1999). In multiple cancer types, altered gene expression of these three urea cycle genes is a prognostic indicator of disease (Allen et al., 2014; Kobayashi et al., 2010; Lan et al., 2014; Lee et al., 2018; Li et al., 2019; Liu et al., 2017; Szlosarek et al., 2006; Vardon et al., 2017). In some p53-deficient cancers, upregulation of urea cycle genes has been shown to be required for the disposal of ammonia generated by rapidly growing tumors as well as provide ornithine for polyamine synthesis to support growth (Li et al., 2019). Collectively, altered expression of urea cycle genes in cancer has been termed urea cycle dysregulation, which produces distinct genomic and biochemical signatures that are observed clinically (Lee et al., 2018).

Catalyzing the first and rate-limiting step in ammonia commitment to the urea cycle, CPS1 plays a central role in supporting both pyrimidine synthesis and ammonia detoxification in cancer (Lee et al., 2018; Li et al., 2019). CPS1 overexpression and activity in LKB1-deficient and EGFR mutant non-small cell lung cancer (NSCLC) has been shown to feed into the pyrimidine biosynthetic pathway to support cancer cell proliferation (Çeliktaş et al., 2017; Kim et al., 2017; Pham-Danis et al., 2019). Here, carbamoyl phosphate generated by CPS1 is consumed by CAD (carbamoyl phosphate synthetase 2 [CPS2], aspartyl transcarbamylase, dihydroorotase) in the pyrimidine synthetic pathway rather than feeding into the urea cycle, which is not active in lung cancer. This shunt of carbamoyl phosphate from CPS1 to CAD presumably bypasses a negative feedback loop of pyrimidine inhibition of CPS2 activity of CAD to allow for sustained and unchecked pyrimidine synthesis to support cancer cell growth (Serre et al., 2004; Shaw and Carrey, 1992). Genetic knockdown of CPS1 was shown to reduce cancer cell proliferation both *in vitro* and *in vivo* and synergize with standard of care NSCLC chemotherapeutics (Çeliktaş et al., 2017; Kim et al., 2017). In addition to supporting pyrimidine synthesis, CPS1 upregulation along with other urea cycle genes has been

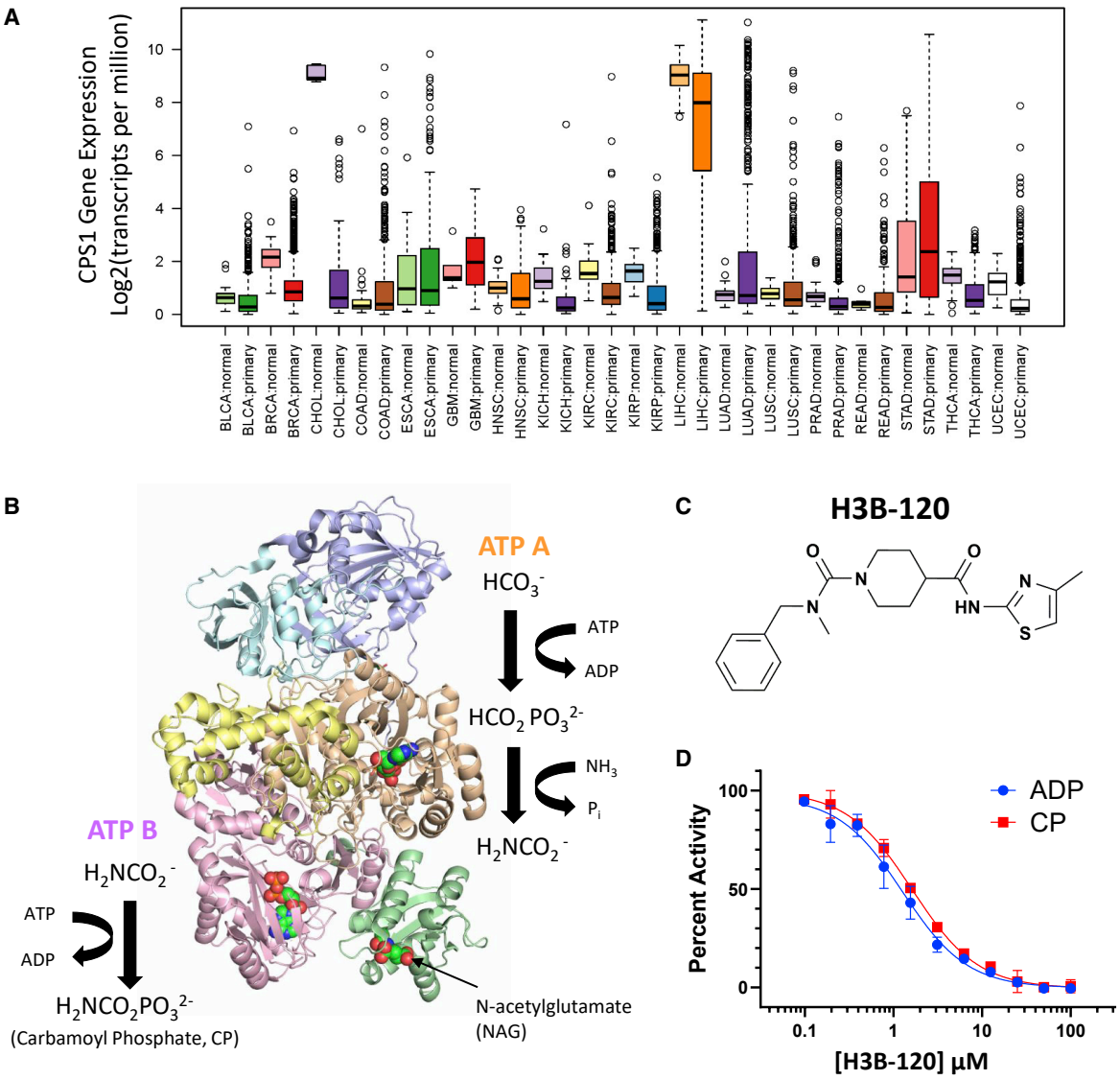

Figure 1. CPS1 Gene Expression in Cancer and the Identification of CPS1 Inhibitor H3B-120

(A) Analysis of CPS1 mRNA expression levels in normal and primary tumor samples from The Cancer Genome Atlas (TCGA) cohort. Only indications with n > 5 samples and with both normal and tumor data were included. Abbreviations for each tumor type correspond to TCGA nomenclature. Boxplots represent CPS1 expression levels between the first and third quartile with the median represented as a horizontal line. Outliers, falling outside of the 1.5 interquartile range, are represented as circles.

(B) Crystal structure of the ADP and NAG bound active conformation of CPS1 (PDB: 5DOU) with an outline of the CPS1 catalyzed carbamoyl phosphate synthesis reaction. CPS1 contains six globular domains: N-terminal domain (light blue), inactive glutamine amido transferase domain (purple), carbamate synthetase ATP A domain (light orange), integrating domain (yellow), carbamoyl phosphate synthetase ATP B domain (pink), and NAG binding domain (green).

(C) Chemical structure of H3B-120.

(D) Dose-response curve of H3B-120 inhibition of CPS1 activity when measuring ADP formation using the PK/LDH assay (IC_{50} = 1.2 µM, Hill coefficient 1.1) or carbamoyl phosphate (CP) production (IC_{50} = 1.6 µM, Hill coefficient 1.0). Error bars represent the standard deviation, n = 2.

demonstrated to prevent the accumulation of high levels of ammonia in p53-deficient malignant cells, which may otherwise be toxic to rapidly growing tumors (Li et al., 2019). Also in this setting, increased nitrogen flux through the urea cycle allows for a higher rate of polyamine synthesis to support growth (Li et al., 2019).

An analysis of CPS1 mRNA expression across all cohorts from The Cancer Genome Atlas (https://portal.gdc.cancer.gov) reveals that CPS1 transcript levels can be upregulated in multiple cancer types (Figure 1A). CPS1 is found to be highly overexpressed in a subset of lung, colon, prostate, bladder, esophageal, and endometrial cancers (Figure 1A). In colon cancer and LKB1-deficient NSCLC, increased CPS1 expression is associated with decreased probability of survival of cancer patients (Kim et al., 2017; Lee et al., 2014; May et al., 2011; Palaniappan et al., 2016; Pham-Danis et al., 2019). Likewise, CPS1

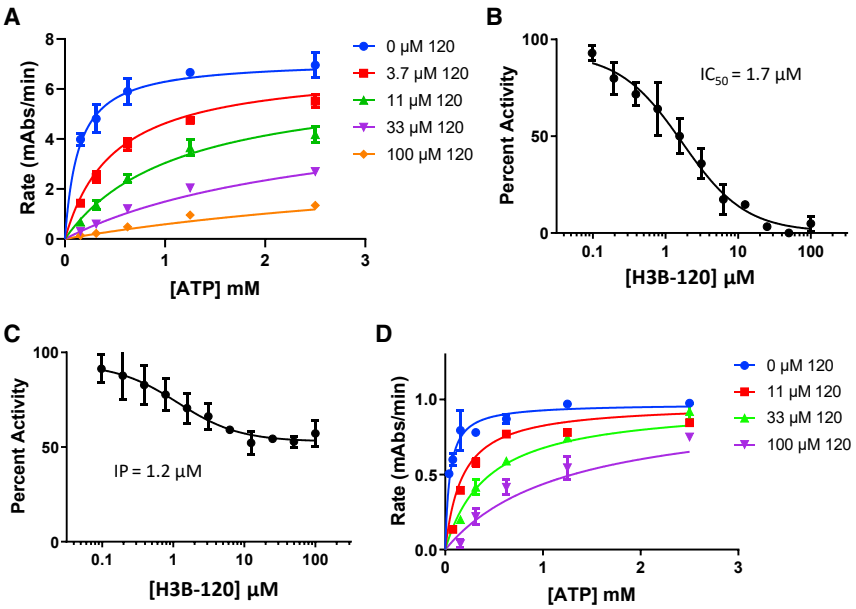

Figure 2. Steady-State Kinetic Analysis of H3B-120 Inhibition of CPS1

(A) Steady-state kinetic analysis of H3B-120 inhibition of total CPS1 activity measured using the PK/LDH assay. Curves are globally fit to a mixed inhibition model. Data presented as a representative graph. Error bars represent the standard deviation, n = 2.

(B) Representative IC_{50} curve of H3B-120 measuring ADP formation only at the ATP A domain using the PK/LDH assay. Error bars represent the standard deviation, n = 2.

(C) Representative IC_{50} curve of H3B-120 inhibition of ATP B activity using the Kinase Glo assay. Error bars represent the standard deviation, n = 2.

(D) Global fit of steady-state kinetic analysis of H3B-120 inhibition of CPS1 ATP A activity using the PK/LDH assay. Data are globally fit to a competitive inhibition model. Error bars represent the standard deviation, n = 2.

overexpression in cholangiocarcinoma and some subtypes of glioblastoma is associated with poor prognosis (Ma et al., 2015; Milinkovic et al., 2013). These observations suggest that increased CPS1 activity may be exploited frequently by malignant cells to support tumor growth in multiple cancer types.

These observations highlight the need to gain a better understanding of the role CPS1 plays in cancer. With no known inhibitors identified to date, we performed a high-throughput screen in search of CPS1 small-molecule inhibitors. Herein, we describe the discovery of a small-molecule inhibitor, H3B-120, which targets a previously unidentified allosteric pocket to achieve inhibition of CPS1 carbamoyl phosphate synthesis activity. Kinetic and structural data demonstrate that H3B-120 causes a conformational change in the carbamate synthetase domain, which prevents ATP binding and catalysis. H3B-120 is selective for CPS1, with no inhibition of CPS2 activity of CAD. H3B-120 is also active in cellular assays, blocking both CPS1 activity in ammonia conversion to urea and support of pyrimidine synthesis. We propose that H3B-120 is a valuable tool for future efforts toward dissecting the involvement of CPS1 in cancer biology.

RESULTS

Identification of a Small-Molecule Inhibitor of CPS1

CPS1 converts ammonia to carbamoyl phosphate in a multistep reaction—consuming ammonia, bicarbonate, and two molecules of ATP for every molecule of carbamoyl phosphate generated (Figure 1B) (de Cima et al., 2015; Diez-Fernandez et al., 2013; Rubio et al., 1979). In the first step of the reaction, carbamate is produced from bicarbonate and ammonia at the expense of one molecule of ATP at the carbamate synthetase domain (hereafter referred to as ATP A). Carbamate is subsequently shuttled through an internal tunnel to the carbamoyl phosphate synthetase domain (hereafter referred to as ATP B), where a second phosphoryl transfer event occurs to generate the final product carbamoyl phosphate (de Cima et al., 2015). Efficient catalysis requires a cofactor, N-acetyl glutamate (NAG). NAG binds to the C-terminal NAG binding domain, causing large structural rearrangements in CPS1 (primarily in the ATP A domain) to form the active conformation (de Cima et al., 2015). In the absence of NAG, CPS1 activity is very low (Britton et al., 1990). CPS1 also contains a small N-terminal domain of unknown function as well as a vestigial glutamine amido transferase domain, which lacks key amino acids required for glutamine hydrolysis. A sixth globular domain referred to as the integrating domain sits between the ATP A and ATP B domains (Figure 1B) (de Cima et al., 2015). The integrating domain stabilizes a portion of the internal tunnel for carbamate transfer from ATP A to ATP B and undergoes some structural rearrangement upon NAG and ATP binding, likely contributing to the stability of the catalytically competent CPS1 conformation.

We developed an enzymatic assay measuring the ADP formation activity of CPS1 and screened a diverse chemical library comprised of approximately 350,000 compounds. H3B-120 was first identified as a confirmed hit following a series of counter screens and biophysical assays that verified direct CPS1 inhibition and binding (Figures 1C, S1, and S2). H3B-120 demonstrated complete inhibition of both ATP activity and carbamoyl phosphate synthetase activity of CPS1 with an half maximal inhibitory concentration (IC_{50}) value of around 1.5 μM (Figure 1D). A steady-state kinetic ATP competition experiment was performed, globally fitting the data to a mixed inhibition model. Here, a K_i of 1.4 μM was determined for H3B-120, in close agreement with measured IC_{50} values (Figure 2A). An α value of 76.7 was calculated, indicating a mixed mode of inhibition for the overall reaction with the inhibitor having higher affinity for the apoenzyme than the enzyme substrate complex.

Determining the Mechanism of Action of H3B-120

Because CPS1 synthesizes carbamoyl phosphate in a multistep process through the coordinated action of two distinct and separate domains with enzymatic activity, we next determined which step of the reaction H3B-120 inhibited. First, we measured activity of the ATP A domain, by simply omitting ammonia from the

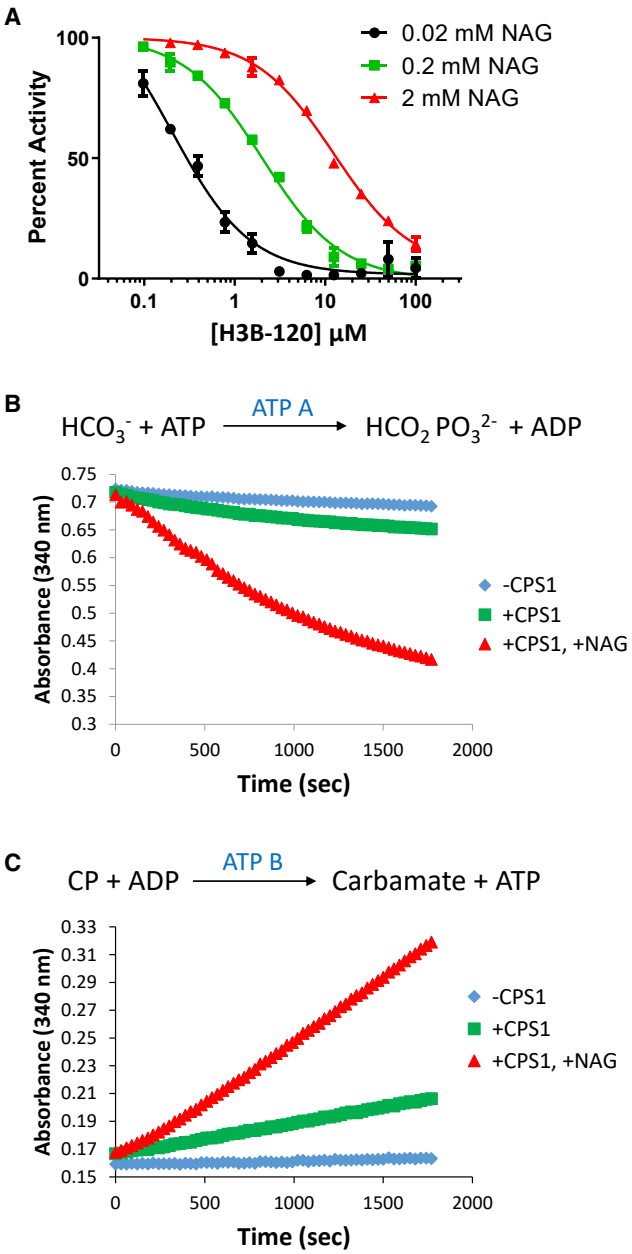

Figure 3. The Effect of NAG Cofactor on CPS1 Activity and Inhibition by H3B-120

(A) IC_{50} curves of H3B-120 measuring CPS1 catalyzed ADP formation from the full reaction at varying concentrations of NAG using the Transcreener FP assay. Error bars represent the standard deviation, n = 2.

(B) The effect of a saturating concentration of NAG on the ADP formation activity of the ATP A domain. ADP formation activity of the ATP A domain was measured continuously for 30 min using a PK/LDH enzyme-coupled assay.

(C) The effect of a saturating concentration of NAG on the ADP formation activity of the ATP B domain. ADP formation activity at ATP B only was measured continuously for 30 min using the HK/G6PDH enzyme-coupled assay.

reaction and measuring ADP formation as carboxyphosphate was generated. H3B-120 was able to fully inhibit this first step, with an IC_{50} essentially identical to the full reaction (Figure 2B). To measure activity of the ATP B domain, we measured ATP synthesis in the reverse direction, using carbamoyl phosphate as the phosphate donor for ADP. H3B-120 was incapable of fully inhibiting ATP B activity, with only partial inhibition observed (Figure 2C). Notably, the inflection point of this curve was 1.2 µM, suggesting that a specific interaction between CPS1 and H3B-120 is responsible for this partial inhibition.

Given the apparent selective inhibition of ATP A activity by H3B-120, we next performed a steady-state kinetic ATP competition experiment in the ATP A half reaction described above. Global fitting of the kinetic data clearly demonstrated competition between ATP and H3B-120, suggesting that binding of these two CPS1 ligands is mutually exclusive (Figure 2D). Unexpectedly, we noticed that when the concentration of NAG was varied in the enzymatic assay measuring the full forward reaction, the IC_{50} of H3B-120 also varied (Figure 3A). As the concentration of NAG is increased, the IC_{50} of H3B-120 inhibition also increased, suggesting competition between H3B-120 and NAG. The apparent competition of H3B-120 with both ATP and NAG was surprising given that ATP and NAG bind to separate domains on the CPS1 protein (de Cima et al., 2015). However, this can be rationalized by the observation that NAG binding influences conformational changes primarily in the ATP A domain to stimulate CPS1 enzymatic activity (de Cima et al., 2015). This is apparent when measuring the ATP activity at each ATP domain separately in the half reactions described above. We observe that a saturating concentration of NAG is able to stimulate activity of the ATP A domain greater than 10-fold (Figure 3B), while NAG activation of ATP B is less than 3-fold (Figure 3C). Collectively, the observed competition between H3B-120 and both ATP and NAG is consistent with two possible models. In the first scenario, H3B-120 directly competes with NAG binding to prevent productive conformational changes at ATP A, selectively blocking activity at this domain. In the second scenario, H3B-120 competes with ATP binding at ATP A, where NAG modulates the affinity for ATP. Here, high concentrations of NAG allow for tighter binding of ATP at the ATP A domain and therefore higher concentrations of H3B-120 are required for competitive inhibition.

CPS1 Inhibitors Bind an Allosteric Pocket between the Integrating and ATP A Domains

To distinguish between these two possible mechanisms we solved a co-crystal structure of CPS1 bound to H3B-193 (Figure 4A), a more potent analog of H3B-120 (Figure S3A), at 1.90 Å resolution. H3B-193 bound CPS1 crystals grew in the previously reported conditions for the apo CPS1 crystal structure. H3B-193 is well resolved in the electron density (Figure S3B) and found sitting in a previously unknown allosteric pocket situated between the integrating and ATP A domains (Figures 4B and S4C). In an overlay of our H3B-193 structure with the ADP bound CPS1 structure (PDB: 5DOU), the phenyl group of H3B-193 is separated from the adenosine ring of ADP within the ATP A domain by ~17 Å. A flexible loop comprised of amino acids V653–H659 (previously referred to as the K-loop [de Cima et al., 2015]) separates these two pockets. In the ADP bound structure, the K-loop is clearly stabilizing ADP binding, with the side chain of M656 interacting with the adenosine ring of ADP (Figure 4C). In the H3B-193 structure, the K-loop is flipped out of the ATP binding pocket of ATP A and toward the

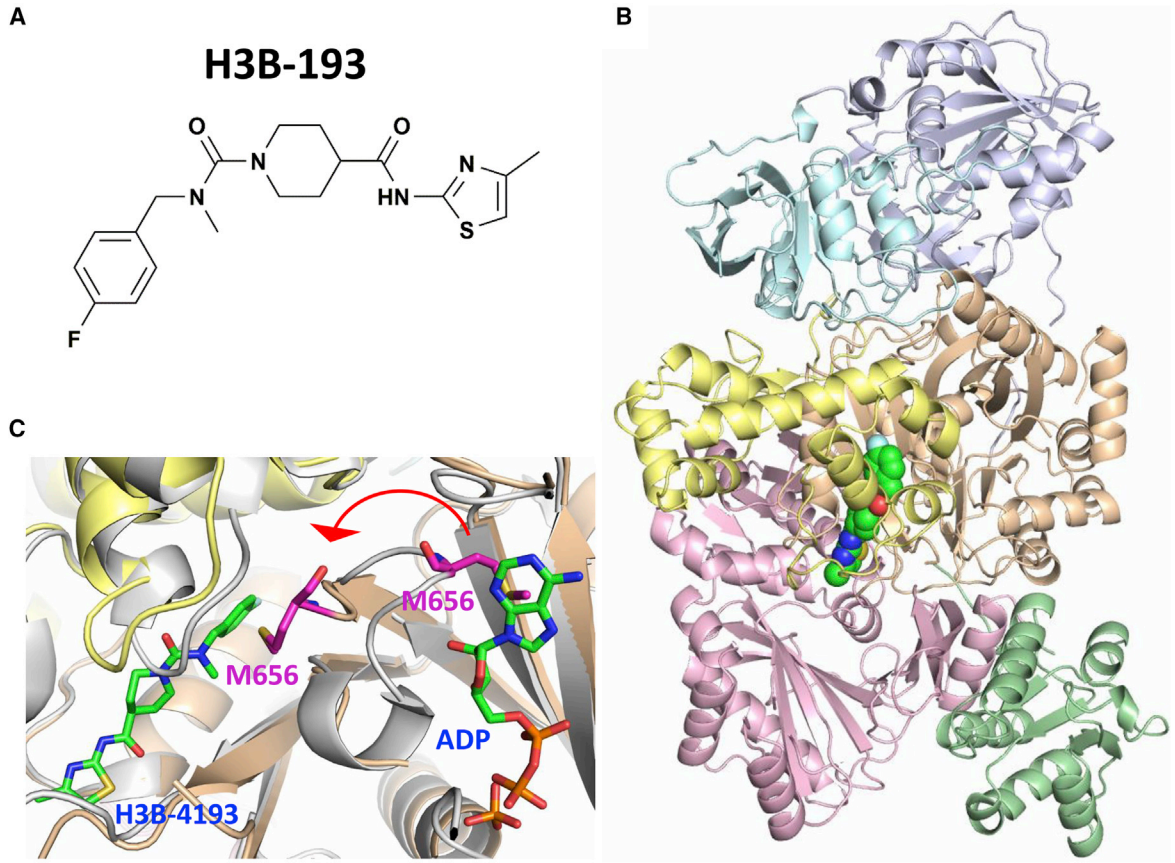

Figure 4. Crystal Structure of CPS1 in Complex with H3B-193

(A) Chemical structure of H3B-193.

(B) Co-crystal structure of the H3B-193-CPS1 complex. H3B-193 is bound to an allosteric pocket between the integrating (yellow) and ATP A (light orange) domains.

(C) H3B-193 binding causes a conformational change in the flexible K-loop that separates the allosteric inhibitor pocket from the ATP binding pocket of the ATP A domain. M656 is observed stabilizing ADP binding the ADP bound CPS1 crystal structure (PDB: 5DOU), but flipped toward H3B-193 to form the allosteric pocket in the inhibitor bound structure. The integrating and ATP A domains of the H3B-193 structure are shown in yellow and light orange, respectively. The ADP bound structure is shown in gray.

allosteric pocket to stabilize H3B-193 binding, with the side chain of M656 reaching into the allosteric pocket (Figure 4C). Inhibitor binding therefore stabilizes the flexible loop in a conformation that is incompatible with ATP binding. This structure fully explains the observed competition between both NAG and ATP in steady-state kinetic experiments. NAG binding enhances CPS1 affinity for ATP at the ATP A domain, where H3B-120 and ATP compete for a CPS1 conformation compatible only with their respective binding modes.

The flexible loop containing amino acids V653–H659 was previously named the K-loop due to its binding of a potassium ion in the ADP bound structure (de Cima et al., 2015). Potassium has been shown to be important specifically for carbamate synthesis at the ATP A domain, but not for enzymatic activity at the ATP B domain (Lusty, 1978, 1983). Potassium was not observed in the H3B-193 structure, suggesting that inhibitor binding stabilizes the K-loop in a conformation that prevents potassium binding and stabilization of the K-loop in a catalytically competent conformation. This likely contributes to the inhibitory mechanism of action of H3B-120 and its analog H3B-193.

The overall conformation of CPS1 in the inhibitor bound structure closely resembles that of the apo structure reported previously, with some movement around the allosteric pocket to accommodate inhibitor binding. The ligand bound allosteric pocket is narrow and long, being roughly 10 Å wide at the opening and 24 Å deep (Figure S3C). A patch of hydrophobic amino acids (M656, V664, F809, L813, and I851) forms the back of the pocket, where the phenyl group of H3B-193 is sandwiched directly between V664 of the ATP A domain and I851 of the integrating domain (Figure 5A). The urea carbonyl oxygen of H3B-193 makes a hydrogen bond with the backbone nitrogen of I851. Two additional hydrogen bonding interactions are mediated by two water molecules bridging side chain hydroxyls of S819 and Y852 with the amide nitrogen and the thiazole nitrogen of H3B-193. The thiazole itself appears to be making an important stacking interaction with the imidazole ring of H817. The pyridine core of H3B-193 sits in the center of the allosteric pocket, between W776 and C816 of the ATP A domain.

To better understand the interactions between CPS1 and inhibitor in the allosteric pocket, we synthesized several structural

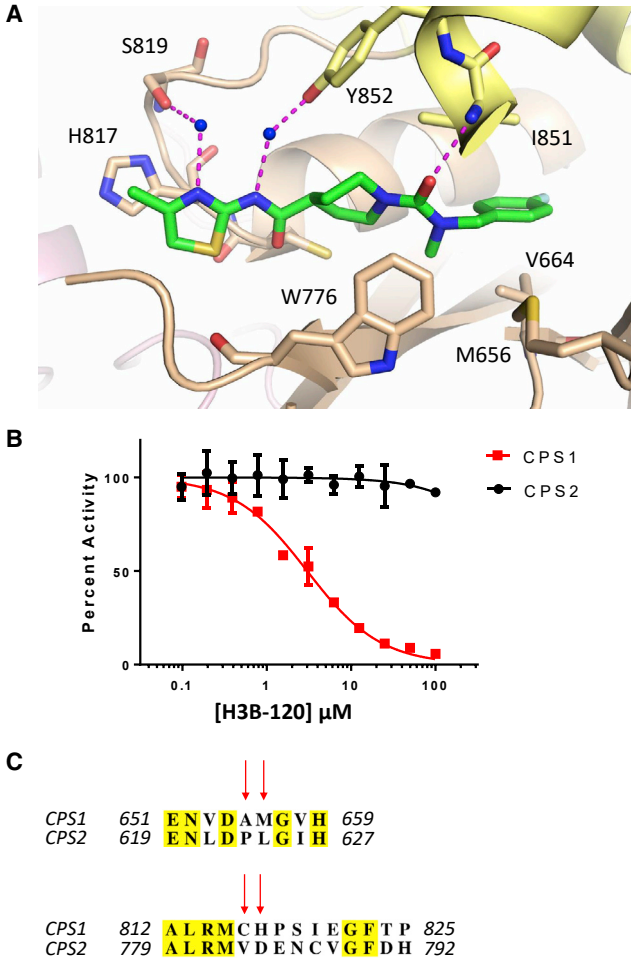

Figure 5. Key Binding Interactions between H3B-193 and CPS1 with Insight into CPS1 Selective Inhibition

(A) Interactions between H3B-193 and CSP1 within the allosteric pocket. H3B-193 engages with amino acids from both the ATP A and integrating domains of CPS1, utilizing hydrogen bonding and hydrophobic interactions to stabilize inhibitor binding.

(B) Representative graph comparing H3B-120 inhibition of CPS1 or CPS2 in the ADP Glo biochemical assay. Error bars represent the standard deviation, n = 2.

(C) Sequence alignment comparing key regions of the allosteric pocket for inhibitor binding between CPS1 and CPS2. Arrows denote key contacts between CPS1 and H3B-193 that are not conserved with CPS2.

analogs of H3B-120 for testing in our biochemical activity assay (Figure S4). Probing the back hydrophobic pocket, we find that small hydrophobic substitutions at the *para* position of the benzyl ring of H3B-120 are favorable, with the addition of both a chloro (cpd 1) and fluoro (H3B-193) having improved affinity over the initial hit, with sub-μM potency. Slightly larger substitutions of a methoxy group at the *para* (cpd 2) and *ortho* (cpd 3) positions were unfavorable, suggesting that the back of the allosteric pocket has limited flexibility to accept larger functional groups. The addition of a methyl group to the amide nitrogen (cpd 4) resulted in a 20-fold reduction in activity, demonstrating the stabilizing effect of the water-mediated interaction with Y852. The importance of the thiazole ring in stabilizing inhibitor binding in the solvent-exposed side of the allosteric pocket is highlighted by the observation that removal of the nitrogen (cpd 5), sulfur (cpd 6), and/or methyl substitution (cpd 7) all resulted in a substantial loss in potency. Together these observations demonstrate the functional importance of the observed interactions between CPS1 and inhibitor in the crystal structure.

H3B-120 Is Highly Selective for CPS1 and Does Not Inhibit the CPS2 Activity of CAD

The only other enzyme in the human genome with known carbamoyl phosphate synthetase activity is CAD (Lane and Fan, 2015). CAD is a large, multifunctional gene responsible for catalyzing the first three steps in the *de novo* pyrimidine synthetic pathway, containing CPS2, aspartyl transcarbamylase, and dihydroorotase activity. CPS1 and CPS2 both utilize bicarbonate and ATP as substrates; however, they differ in their use of a nitrogen source. While CPS1 utilizes ammonia directly, CPS2 instead uses glutamine as a source of nitrogen, hydrolyzing glutamine to ammonia and glutamate at its N-terminal glutamine amido transferase domain. To determine if H3B-120 was selective for CPS1 inhibition, we developed a biochemical assay to measure the CPS2 activity of CAD (Figure S5). Although H3B-120 robustly inhibited CPS1 as described above, there was no appreciable inhibition of CPS2 observed, even at the highest inhibitor concentration tested of 70 μM (Figure 5B). There is no known crystal structure of CPS2 to directly compare the architecture of the H3B-120 allosteric binding pocket of CPS1 with the analogous region of CPS2. However, a sequence alignment between CPS1 and CPS2 reveals a number of key amino acids responsible for forming the allosteric pocket in CPS1 are not conserved in CPS2 (Figure 5C). Notably, the flexible K-loop separating the allosteric pocket and the ATP binding pocket of the ATP A domain contains several differences, with A655 and M656 of CPS1 being found as proline and leucine, respectively, in CPS2. In addition, H817 of CPS1, which forms the key stacking interaction with the thiazole of H3B-193, is replaced with aspartate in CPS2 (Figure 5C). C816, which lines the inhibitor binding pocket of CPS1, is converted to valine in CPS2. These key differences likely explain why H3B-120 is exquisitely selective for CPS1.

H3B-120 and Its Structural Analogs Demonstrate Inhibition of CPS1 Cellular Activity

To determine if H3B-120 was capable of inhibiting cellular CPS1 activity, we measured the ability of H3B-120 to block urea production from primary human hepatocytes by measuring urea secretion into conditioned media from treated cells. H3B-120 was able to inhibit urea production in a dose-dependent manner, although the cellular potency decreased significantly compared with enzymatic assays (Figure 6A). This can be attributed to the poor metabolic stability of H3B-120 in human hepatocytes. The half-life of H3B-120 was measured to be only 40 min, while hepatocytes needed to be incubated for 16 h after H3B-120 treatment to allow sufficient time to secrete enough urea for quantification. Next, we tested a series of biochemically active and inactive H3B-120 analogs in the hepatocyte urea production assay (Figure S4). All biochemically active H3B-120 analogs also showed dose-dependent inhibition of urea secretion, while all biochemically inactive analogs had no cellular activity as

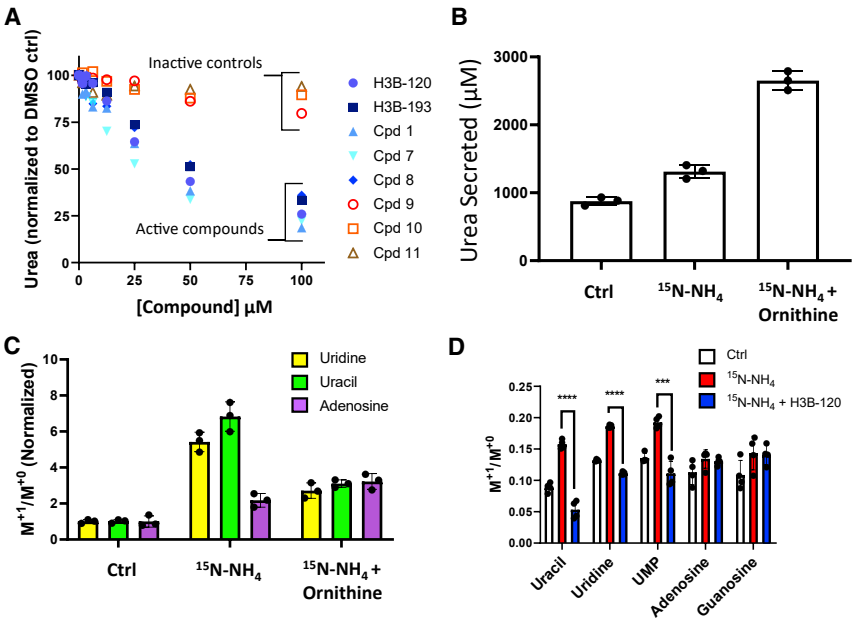

Figure 6. Targeted Cellular Inhibition of Urea and Pyrimidine Synthesis with H3B-120 and Its Structural Analogs

(A) Inhibition of urea production from primary human hepatocytes by H3B-120 and its analogs. Primary human hepatocytes were incubated with 10 mM NH_4Cl in the presence of compound at the indicated concentration. Urea secreted into the media was measured after 16 h.

(B) Urea production was measured at 16 h from hepatocytes treated in the presence or absence of 10 mM ^{15}N-NH_4Cl or 10 mM ^{15}N-NH_4Cl with 10 mM ornithine. Error bars represent the standard deviation, n = 3.

(C) Targeted MetID of pyrimidines uridine and uracil as well as the purine adenosine from cell lysates from (B). Error bars represent the standard deviation, n = 3. The M^{+1}/M^{+0} ratio represents the ratio of labeled to unlabeled metabolite. The M^{+1}/M^{+0} of the control sample represents the ratio of naturally abundant carbon-13 to carbon-12. Control sample data are normalized to 1.

(D) Targeted MetID of pyrimidines and purines in human hepatocytes after treatment with 10 mM ^{15}N-NH_4Cl in the presence or absence of 20 µM H3B-120 for 2 h. Error bars represent the standard deviation, n = 4.

expected (Figure 6A). This provides confidence that H3B-120 and its active analogs are blocking urea production through targeted cellular inhibition of CPS1.

Hepatocytes represent an attractive cellular model for testing CPS1 inhibitors because, in addition to being required for urea production, CPS1 activity has also been reported to feed into pyrimidine synthesis when hepatocytes are stressed with high concentrations of ammonia (Bachmann and Colombo, 1980; Monks et al., 1985; Natale and Tremblay, 1969; Pausch et al., 1985; Tremblay et al., 1977). To verify that a metabolic link between CPS1 and pyrimidine synthesis does exist in primary human hepatocytes, we treated hepatocytes with ^{15}N-labeled ammonia in the presence and absence of ornithine. Ornithine is an essential and limiting metabolite in the urea cycle that has been shown to stimulate urea production when added to the conditioned media of cultured hepatocytes (Cohen et al., 1980). When measuring urea production, we find that the addition of 10 mM ^{15}N ammonia to the media stimulates urea secretion about 30% over standard media during a 16-h period, while the addition of 10 mM ^{15}N ammonia with 10 mM ornithine further increases urea production more than 2-fold over standard media, confirming that ornithine stimulates the urea cycle (Figure 6B). Harvesting hepatocytes from the same experiment and performing targeted MetID on pyrimidines uridine and uracil reveals that ammonia treatment alone significantly enhanced labeling of these two metabolites (Figure 6C). In contrast, concurrent treatment with ornithine significantly decreased pyrimidine labeling relative to ammonia treatment alone. In the same experiment, ornithine had no effect on labeling of the purine adenosine. This experiment demonstrates that the urea cycle and pyrimidine biosynthetic pathway compete for carbamoyl phosphate generated by CPS1, confirming that CPS1 activity can support pyrimidine synthesis in hepatocytes under high ammonia conditions.

Having established that CPS1 activity can support pyrimidine synthesis in primary human hepatocytes, we next tested the ability of H3B-120 to block pyrimidine labeling in hepatocytes treated with ^{15}N-ammonia. Cultured hepatocytes were treated with 10 mM ^{15}N-labeled ammonia in the presence and absence of H3B-120 for 2 h before harvesting the cells. Targeted MetID reveals H3B-120 was able to fully block labeling of the pyrimidines uracil, uridine, and uridine monophosphate, while having no effect on purines adenosine and guanosine (Figure 6D). This experiment further demonstrates the targeted cellular inhibition of CPS1 by H3B-120 and establishes that H3B-120 can fully inhibit CPS1 cellular activity at shorter time points.

DISCUSSION

In this study, we describe the discovery of a small-molecule inhibitor of a carbamoyl phosphate synthetase, CPS1. Biochemical assays demonstrate that H3B-120 effectively blocks carbamate synthesis at the ATP A domain in the first step of carbamoyl phosphate synthesis. An inhibitor bound CPS1 co-crystal structure reveals that H3B-120 achieves inhibition by binding to a previously unknown allosteric pocket situated between the integrating and ATP A domains, likely stabilizing CPS1 in an inactive conformation. The allosteric pocket is immediately adjacent to the ATP binding pocket of the ATP A domain, separated by a single flexible loop comprised of amino acids V653–H659 (the K-loop). In an ADP bound structure, the K-loop stabilizes the adenosine ring of ADP, while in the inhibitor bound structure the K-loop is flipped out of the ATP binding pocket and into the allosteric pocket to stabilize inhibitor binding. The side chain of M656 of the K-loop is observed interacting with the adenosine ring of ADP in the ADP bound structure, but extends into the allosteric pocket in the inhibitor bound structure. This co-crystal structure fully satisfies the surprising observation that H3B-120

appears to compete with both ATP and NAG binding in steady-state kinetic experiments. H3B-120 and ATP do not compete for the same binding site, but rather compete for a CPS1 conformation compatible only with their respective binding mode. Because NAG modulates the affinity of CPS1 for ATP at the ATP A domain, higher concentrations of inhibitor are required to achieve CPS1 inhibition under high NAG conditions.

The allosteric mechanism of action of H3B-120 likely accounts for its observed exquisitely selective inhibition of CPS1 over CPS2 activity of CAD. Although no structure of CPS2 has been solved, this selectivity can probably be attributed to key amino acid differences found in the allosteric pocket, including within the flexible K-loop that separates the allosteric pocket from the ATP binding pocket of the ATP A domain. When considering the possibility of developing a CPS1-targeted inhibitor for the treatment of tumors depending on CPS1 for growth, selective inhibition of CPS1 activity will be highly desirable. All tissues express and depend on CAD for *de novo* pyrimidine synthesis, therefore, a non-selective CPS1/CPS2 inhibitor would likely encounter issues with toxicity.

In summary, the discovery of H3B-120 represents an important first step toward the development of potent, drug-like small-molecule inhibitors of CPS1. Although the potency and metabolic stability of H3B-120 will need to be improved before an *in vivo* ready compound is available, H3B-120 and its analogs now provide researchers with chemical tools to interrogate CPS1 biology *in vitro*. These chemical probes offer potential advantages over genetic methods, including better selectivity than small interfering RNA or short hairpin RNA and reversibility that is not possible with stable knockdown or knockout of CPS1. Hopefully, after additional target validation, CPS1-targeted inhibitors can eventually be developed to treat cancers that depend on CPS1 for growth.

SIGNIFICANCE

Carbamoyl phosphate synthetase 1 (CPS1) catalyzes the first and rate-limiting step in the urea cycle, converting ammonia, bicarbonate, and ATP to carbamoyl phosphate. CPS1 is highly overexpressed in a number of cancers, including LKB1-deficient lung cancer, where CPS1 activity has been demonstrated to promote tumor growth through the support of pyrimidine synthesis. In p53-deficient cancers, CPS1 overexpression has been shown to be required for the removal of ammonia that may otherwise be toxic to growing tumors. These observations highlight the need for the identification of small-molecule inhibitors to probe CPS1 cancer biology. In this study, we describe the discovery of a small-molecule inhibitor of CPS1. From a high-throughput screen we identify H3B-120, which achieves inhibition of CPS1 by blocking bicarbonate phosphorylation in the first step of carbamoyl phosphate synthesis. Steady-state kinetic experiments reveal inhibition of bicarbonate phosphorylation occurs through competition between H3B-120 and ATP. A high-resolution co-crystal structure demonstrates that an analog of H3B-120 binds to a previously unidentified allosteric pocket located between integrating domain and the carbamate synthetase domain of CPS1. A flexible loop that is normally involved in stabilizing ATP binding is observed forming the allosteric, inhibitor bound pocket. The allosteric mechanism of action of H3B-120 allows for highly selective CPS1 inhibition, with no inhibition of CPS2 observed. Analogs of H3B-120 with increased potency are described, which are able to inhibit CPS1 cellular activity, blocking both urea synthesis and CPS1 support of the pyrimidine biosynthetic pathway. H3B-120 and its analogs are valuable tools for probing CPS1 biology.

STAR★METHODS

Detailed methods are provided in the online version of this paper and include the following:

- KEY RESOURCES TABLE
- LEAD CONTACT AND MATERIALS AVAILABILITY
- EXPERIMENTAL MODEL AND SUBJECT DETAILS
  - Cell Lines
- METHODS DETAILS
  - Protein Expression and Purification
  - PK/LDH Coupled Assay
  - ADP-Glo® Assay
  - Transcreener ADP2 FP® Assay
  - Carbamoyl Phosphate Detection Assay
  - Carboxy Phosphate Synthesis (ATP A) Activity Assay
  - Carbamate/ATP Synthesis (ATP B) Activity Assay
  - Equations
  - CAD (CPS2) Activity Assay
  - Differential Scanning Fluorimetery (DSF)
  - Ligand Detection NMR Experiments
  - Crystallization and Structure Determination
  - Hepatocyte Urea Production Assay
  - MetID
- QUANTIFICATION AND STATISTICAL ANALYSIS
- DATA AND CODE AVAILABILITY

SUPPLEMENTAL INFORMATION

Supplemental Information can be found online at https://doi.org/10.1016/j.chembiol.2020.01.009.

ACKNOWLEDGMENTS

We thank all employees of H3 Biomedicine Inc for their helpful discussions related to this project.

AUTHOR CONTRIBUTIONS

S.Y., T.-V.N., A.A.A., S.Y., P.B., and J.W. collected and analyzed the data. S.P., J.K., F.C., K.C.H., X.B., K.O., A.S., L.Y., S.I., F.H.V., and P.Z. analyzed the data. A.R. designed and synthesized compounds and analyzed the data. N.A.L and D.M.B analyzed the data and wrote the manuscript.

DECLARATION OF INTERESTS

Competing interests: S.Y., T.-V.N., A.R., A.A.A., J.K., S.P., F.C., J.W., K.C.H., X.B., K.O., A.S., L.Y., S.I., F.H.V., P.Z., N.A.L., and D.M.B. are current or former employees of H3 Biomedicine. S.Y. and P.B. declare no competing interest.

Received: October 23, 2019
Revised: December 9, 2019
Accepted: January 13, 2020
Published: February 3, 2020

REFERENCES

Adeva, M.M., Souto, G., Blanco, N., and Donapetry, C. (2012). Ammonium metabolism in humans. Metabolism *61*, 1495–1511.

Allen, M.D., Luong, P., Hudson, C., Leyton, J., Delage, B., Ghazaly, E., Cutts, R., Yuan, M., Syed, N., Lo Nigro, C., et al. (2014). Prognostic and therapeutic impact of argininosuccinate synthetase 1 control in bladder cancer as monitored longitudinally by PET imaging. Cancer Res. *74*, 896–907.

Bachmann, C., and Colombo, J.P. (1980). Diagnostic value of orotic acid excretion in heritable disorders of the urea cycle and in hyperammonemia due to organic acidurias. Eur. J. Pediatr. *134*, 109–113.

Britton, H.G., García-España, A., Goya, P., Rozas, I., and Rubio, V. (1990). A structure-reactivity study of the binding of acetylglutamate to carbamoyl phosphate synthetase I. Eur. J. Biochem. *188*, 47–53.

Brosnan, M.E., and Brosnan, J.T. (2007). Orotic acid excretion and arginine metabolism. J. Nutr. *137*, 1656S–1661S.

Çeliktaş, M., Tanaka, I., Chandra Tripathi, S., Fahrmann, J.F., Aguilar-Bonavides, C., Villalobos, P., Delgado, O., Dhillon, D., Dennison, J.B., Ostrin, E.J., et al. (2017). Role of CPS1 in cell growth, metabolism, and prognosis in LKB1-inactivated lung adenocarcinoma. J. Natl. Cancer Inst. *109*, djw231.

de Cima, S., Polo, L.M., Díez-Fernández, C., Martínez, A.I., Cervera, J., Fita, I., and Rubio, V. (2015). Structure of human carbamoyl phosphate synthetase: deciphering the on/off switch of human ureagenesis. Sci. Rep. *5*, 16950.

Clabbers, M.T.B., Gruene, T., Parkhurst, J.M., Abrahams, J.P., and Waterman, D.G. (2018). Electron diffraction data processing with DIALS. Acta Crystallogr. D Struct. Biol. *74*, 506–518.

Cohen, N.S., Cheung, C.W., and Raijman, L. (1980). The effects of ornithine on mitochondrial carbamyl phosphate synthesis. J. Biol. Chem. *255*, 10248–10255.

Diez-Fernandez, C., Martínez, A.I., Pekkala, S., Barcelona, B., Pérez-Arellano, I., Guadalajara, A.M., Summar, M., Cervera, J., and Rubio, V. (2013). Molecular characterization of carbamoyl-phosphate synthetase (CPS1) deficiency using human recombinant CPS1 as a key tool. Hum. Mutat. *34*, 1149–1159.

Emsley, P., Lohkamp, B., Scott, W.G., and Cowtan, K. (2010). Features and development of Coot. Acta Crystallogr. D Biol. Crystallogr. *66*, 486–501.

Gerrits, G.P., Gabreëls, F.J., Monnens, L.A., De Abreu, R.A., van Raaij-Selten, B., Niezen-Koning, K.E., and Trijbels, J.M. (1993). Argininosuccinic aciduria: clinical and biochemical findings in three children with the late onset form, with special emphasis on cerebrospinal fluid findings of amino acids and pyrimidines. Neuropediatrics *24*, 15–18.

Guy, H.I., and Evans, D.R. (1994). Cloning and expression of the mammalian multifunctional protein CAD in *Escherichia coli*. Characterization of the recombinant protein and a deletion mutant lacking the major interdomain linker. J. Biol. Chem. *269*, 23808–23816.

Keshet, R., Szlosarek, P., Carracedo, A., and Erez, A. (2018). Rewiring urea cycle metabolism in cancer to support anabolism. Nat. Rev. Cancer *18*, 634–645.

Kim, J., Hu, Z., Cai, L., Li, K., Choi, E., Faubert, B., Bezwada, D., Rodriguez-Canales, J., Villalobos, P., Lin, Y.-F., et al. (2017). CPS1 maintains pyrimidine pools and DNA synthesis in KRAS/LKB1-mutant lung cancer cells. Nature *546*, 168–172.

Kobayashi, E., Masuda, M., Nakayama, R., Ichikawa, H., Satow, R., Shitashige, M., Honda, K., Yamaguchi, U., Shoji, A., Tochigi, N., et al. (2010). Reduced argininosuccinate synthetase is a predictive biomarker for the development of pulmonary metastasis in patients with osteosarcoma. Mol. Cancer Ther. *9*, 535–544.

van Kuilenburg, A.B.P., van Maldegem, B.T., Abeling, N.G.G.M., Wijburg, F.A., and Duran, M. (2006). Analysis of pyrimidine synthesis de novo intermediates in urine during crisis of a patient with ornithine transcarbamylase deficiency. Nucleosides Nucleotides Nucleic Acids *25*, 1251–1255.

Lan, J., Tai, H.-C., Lee, S.-W., Chen, T.-J., Huang, H.-Y., and Li, C.-F. (2014). Deficiency in expression and epigenetic DNA Methylation of ASS1 gene in nasopharyngeal carcinoma: negative prognostic impact and therapeutic relevance. Tumour Biol. *35*, 161–169.

Lane, A.N., and Fan, T.W.-M. (2015). Regulation of mammalian nucleotide metabolism and biosynthesis. Nucleic Acids Res. *43*, 2466–2485.

Lee, J.S., Adler, L., Karathia, H., Carmel, N., Rabinovich, S., Auslander, N., Keshet, R., Stettner, N., Silberman, A., Agemy, L., et al. (2018). Urea cycle dysregulation generates clinically relevant genomic and biochemical signatures. Cell *174*, 1559–1570.e22.

Lee, Y.-Y., Li, C.-F., Lin, C.-Y., Lee, S.-W., Sheu, M.-J., Lin, L.-C., Chen, T.-J., Wu, T.-F., and Hsing, C.-H. (2014). Overexpression of CPS1 is an independent negative prognosticator in rectal cancers receiving concurrent chemoradiotherapy. Tumour Biol. *35*, 11097–11105.

Levine, R.L., and Kretchmer, N. (1971). Conversion of carbamoyl phosphate to hydroxyurea. An assay for carbamoylphosphate synthetase. Anal. Biochem. *42*, 324–337.

Li, L., Mao, Y., Zhao, L., Li, L., Wu, J., Zhao, M., Du, W., Yu, L., and Jiang, P. (2019). p53 regulation of ammonia metabolism through urea cycle controls polyamine biosynthesis. Nature *567*, 253–256.

Liu, Q., Stewart, J., Wang, H., Rashid, A., Zhao, J., Katz, M.H., Lee, J.E., Fleming, J.B., Maitra, A., Wolff, R.A., et al. (2017). Reduced expression of argininosuccinate synthetase 1 has a negative prognostic impact in patients with pancreatic ductal adenocarcinoma. PLoS One *12*, e0171985.

Lusty, C.J. (1978). Carbamyl phosphate synthetase. Bicarbonate-dependent hydrolysis of ATP and potassium activation. J. Biol. Chem. *253*, 4270–4278.

Lusty, C.J. (1983). The molecular structure and function of carbamyl phosphate synthetase I. Trans. N. Y. Acad. Sci. *41*, 103–115.

Ma, S.-L., Li, A.-J., Hu, Z.-Y., Shang, F.-S., and Wu, M.-C. (2015). Co-expression of the carbamoyl-phosphate synthase 1 gene and its long non-coding RNA correlates with poor prognosis of patients with intrahepatic cholangiocarcinoma. Mol. Med. Rep. *12*, 7915–7926.

May, D., Pan, S., Crispin, D.A., Lai, K., Bronner, M.P., Hogan, J., Hockenbery, D.M., McIntosh, M., Brentnall, T.A., and Chen, R. (2011). Investigating neoplastic progression of ulcerative colitis with label-free comparative proteomics. J. Proteome Res. *10*, 200–209.

Milinkovic, V., Bankovic, J., Rakic, M., Stankovic, T., Skender-Gazibara, M., Ruzdijic, S., and Tanic, N. (2013). Identification of novel genetic alterations in samples of malignant glioma patients. PLoS One *8*, e82108.

Monks, A., Chisena, C.A., and Cysyk, R.L. (1985). Influence of ammonium ions on hepatic de novo pyrimidine biosynthesis. Arch. Biochem. Biophys. *236*, 1–10.

Murshudov, G.N., Vagin, A.A., and Dodson, E.J. (1997). Refinement of macromolecular structures by the maximum-likelihood method. Acta Crystallogr. D Biol. Crystallogr. *53*, 240–255.

Natale, P.J., and Tremblay, G.C. (1969). On the availability of intramitochondrial carbamoylphosphate for the extramitochondrial biosynthesis of pyrimidines. Biochem. Biophys. Res. Commun. *37*, 512–517.

Palaniappan, A., Ramar, K., and Ramalingam, S. (2016). Computational identification of novel stage-specific biomarkers in colorectal cancer progression. PLoS One *11*, e0156665.

Pausch, J., Rasenack, J., Häussinger, D., and Gerok, W. (1985). Hepatic carbamoyl phosphate metabolism. Role of cytosolic and mitochondrial carbamoyl phosphate in de novo pyrimidine synthesis. Eur. J. Biochem. *150*, 189–194.

Pham-Danis, C., Gehrke, S., Danis, E., Rozhok, A.I., Daniels, M.W., Gao, D., Collins, C., Paola, J.T.D., D'Alessandro, A., and DeGregori, J. (2019). Urea cycle sustains cellular energetics upon EGFR inhibition in EGFR-mutant NSCLC. Mol. Cancer Res. *17*, 1351–1364.

Pierson, D.L. (1980). A rapid colorimetric assay for carbamyl phosphate synthetase I. J. Biochem. Biophys. Methods *3*, 31–37.

Rabinovich, S., Adler, L., Yizhak, K., Sarver, A., Silberman, A., Agron, S., Stettner, N., Sun, Q., Brandis, A., Helbling, D., et al. (2015). Diversion of aspartate in ASS1-deficient tumours fosters de novo pyrimidine synthesis. Nature *527*, 379–383.

Rubio, V., Britton, H.G., and Grisolia, S. (1979). Mechanism of carbamoylphosphate synthetase. Binding of ATP by the rat-liver mitochondrial enzyme. Eur. J. Biochem. *93*, 245–256.

Salerno, C., D'Eufemia, P., Celli, M., Finocchiaro, R., Crifò, C., and Giardini, O. (1999). Determination of urinary orotic acid and uracil by capillary zone electrophoresis. J. Chromatogr. B Biomed. Sci. Appl. *734*, 175–178.

Serre, V., Penverne, B., Souciet, J.-L., Potier, S., Guy, H., Evans, D., Vicart, P., and Hervé, G. (2004). Integrated allosteric regulation in the *S. cerevisiae* carbamylphosphate synthetase-aspartate transcarbamylase multifunctional protein. BMC Biochem. *5*, 6.

Shaw, S.M., and Carrey, E.A. (1992). Regulation of the mammalian carbamoylphosphate synthetase II by effectors and phosphorylation. Altered affinity for ATP and magnesium ions measured using the ammonia-dependent part reaction. Eur. J. Biochem. *207*, 957–965.

Szlosarek, P.W., Klabatsa, A., Pallaska, A., Sheaff, M., Smith, P., Crook, T., Grimshaw, M.J., Steele, J.P., Rudd, R.M., Balkwill, F.R., et al. (2006). In vivo loss of expression of argininosuccinate synthetase in malignant pleural mesothelioma is a biomarker for susceptibility to arginine depletion. Clin. Cancer Res. *12*, 7126–7131.

Tremblay, G.S., Crandall, D.E., Knott, C.E., and Alfant, M. (1977). Orotic acid biosynthesis in rat liver: studies on the source of carbamoylphosphate. Arch. Biochem. Biophys. *178*, 264–277.

Vardon, A., Dandapani, M., Cheng, D., Cheng, P., De Santo, C., and Mussai, F. (2017). Arginine auxotrophic gene signature in paediatric sarcomas and brain tumours provides a viable target for arginine depletion therapies. Oncotarget *8*, 63506–63517.

Vedadi, M., Niesen, F.H., Allali-Hassani, A., Fedorov, O.Y., Finerty, P.J., Wasney, G.A., Yeung, R., Arrowsmith, C., Ball, L.J., Berglund, H., et al. (2006). Chemical screening methods to identify ligands that promote protein stability, protein crystallization, and structure determination. Proc. Natl. Acad. Sci. U S A *103*, 15835–15840.

Winter, G., Waterman, D.G., Parkhurst, J.M., Brewster, A.S., Gildea, R.J., Gerstel, M., Fuentes-Montero, L., Vollmar, M., Michels-Clark, T., Young, I.D., et al. (2018). DIALS: implementation and evaluation of a new integration package. Acta Crystallogr. D Struct. Biol. *74*, 85–97.

STAR★METHODS

KEY RESOURCES TABLE

REAGENT or RESOURCE	SOURCE	IDENTIFIER
Chemicals, Peptides, and Recombinant Proteins		
His-CPS1	This Paper	N/A
His-CAD	This Paper	N/A
Pyruvate Kinase, Lactate Dehydrogenase	Sigma Aldrich	Cat# P0294
Hexokinase, Glucose-6-phosphate Dehydrogenase	Sigma Aldrich	Cat# 10127825001
Critical Commercial Assays		
ADP-Glo	Promega	Cat# V9102
Transcreener ADP2 FP	Bellbrook Labs	Cat# 3010
Kinase-Glo	Promega	Cat# V6713
Deposited Data		
CPS1 bound to H3B-193	This Paper	PDB: 6UEL
Ligand bound CPS1	(de Cima et al., 2015)	PDB: 5DOU
Apo CPS1	(de Cima et al., 2015)	PDB: 5DOT
Experimental Models: Cell Lines		
Primary Male Human Hepatocytes	BioIVT	Cat# M00995-P
Recombinant DNA		
His-CPS1 pET28b	Genewiz	N/A
His-CAD pET28b	Genewiz	N/A
Software and Algorithms		
GraphPad Prism	GraphPad Prism Inc	N/A
DIALS	(Clabbers et al., 2018; Winter et al., 2018)	N/A
COOT	(Emsley et al., 2010)	N/A
REFMAC5	(Murshudov et al., 1997)	N/A
PyMOL	Schrodinger, LLC	N/A
ChemDraw	PerkinElmer	N/A

LEAD CONTACT AND MATERIALS AVAILABILITY

Requests for resources and reagents should be directed to the Lead Contact: David Bolduc (david_bolduc@h3biomedicine.com). The reagents generated in this study will be made available with a completed Materials Transfer Agreement.

EXPERIMENTAL MODEL AND SUBJECT DETAILS

Cell Lines

Source of Cell Lines

Primary human hepatocytes (gender: male) were purchased from BioIVT. Primary hepatocytes were cultured in InVitroGro CP medium (BioIVT, cat # Z99029) supplemented with Torpedo antibiotic mix (BioIVT cat # Z99000). Cells were maintained on collagen coated plates (Fisher, cat# 08-774-5) in a 37°C, 5% CO_2 incubator.

METHODS DETAILS

Protein Expression and Purification

CPS1 was expressed in SF21 insect cells as described previously (de Cima et al., 2015). Briefly, the full length CPS1 gene was cloned into pFastBac HTA and baculovirus was generated using the Bac-to-bac expression system from Invitrogen. P3 virus was used to infect SF21 insect cells at a density of 1.5E6 cells/mL at an MOI of 2. The infection was allowed to proceed for 60 hrs before the cells were harvested by centrifugation. The cell pellet was resuspended in lysis buffer (50 mM glycyl glycine pH 7.4, 20 mM KCl, 1 mM TCEP, 10% glycerol and 20 mM imidazole with Roche protease inhibitor tablet) before being lysed using

a Dounce homogenizer. The lysate was then centrifuged at 30,000 rpm for 30 min to remove insoluble cell debris. 40 mL of supernatant was mixed with 2 mL of Ni NTA beads for 45 min at 4°C in a 50 mL conical tube. After binding, the beads were washed three times with 40 mL of wash buffer (50 mM glycyl glycine pH 7.4, 500 mM NaCl, 1 mM TCEP, 10% glycerol and 50 mM imidazole) by repeated centrifugation and resuspension of the beads. CPS1 protein was eluted three times in 6 mL of elution buffer (50 mM glycyl glycine pH 7.4, 500 mM NaCl, 1 mM TCEP, 10% glycerol and 250 mM imidazole. Elution fractions were combined and concentrated. Imidazole was removed by repeated concentration and resuspension in storage buffer (50 mM glycyl glycine pH 7.4, 500 mM NaCl, 1 mM TCEP and 20% glycerol). CPS1 was concentrated to ~3 mg/mL before being frozen in liquid nitrogen for storage at -80°C. This procedure yielded approximately 10 mg/L CPS1 with a purity of >95%. Using the PK/LDH assay described below to measure ADP formation, k_{cat} for purified CPS1 was determined to be 44.7 min^{-1}.

Recombinant CAD was expressed in *E. coli* as described previously (Guy and Evans, 1994). Briefly, CAD was cloned into the pET28b expression vector and transformed into BL21 (DE3) cells for expression. 2 L of LB broth was inoculated with a 4 mL overnight culture. The 2 L culture was grown at 37°C until an OD of 0.8 was reached, at which point 1 mM IPTG was added to induce CAD expression and the cultures cooled to 16°C for overnight expression. The following day cultures were pelleted by centrifugation. Cell pellets were resuspended in lysis buffer (50 mM Tris pH 8.0, 500 mM NaCl, 1 mM TCEP, 10% glycerol and 20 mM imidazole) and lysed by sonication (30 sec, 60% amplitude, 3 times). Cell debris was cleared by centrifugation and 40 mL of the supernatant mixed with 1 mL Ni NTA beads in a 50 mL conical tube for 40 min. The Ni beads were washed with wash buffer (50 mM Tris pH 8.0, 500 mM NaCl, 1 mM TCEP, 10% glycerol and 50 mM imidazole) three times by centrifugation and resuspension of the beads. CAD was eluted three times in elution buffer (50 mM Tris pH 8.0, 500 mM NaCl, 1 mM TCEP, 10% glycerol and 250 mM imidazole). Pure fractions were then concentrated and imidazole removed by repeated concentration and dilution in storage buffer (50 mM Tris pH 8.0, 500 mM NaCl, 1 mM TCEP and 20% glycerol). CAD was stored at -80°C at a concentration of ~1 mg/mL. This procedure yielded approximately 0.3 mg/L CAD with a purity of >90%. Using the PK/LDH assay described below to measure ADP formation from CAD, k_{cat} for CPS2 was determined to be 16.5 min^{-1}.

PK/LDH Coupled Assay

CPS1 activity was measured continuously as ADP was produced in a pyruvate kinase/lactate dehydrogenase enzyme coupled assay. 50 nM CPS1 was incubated in assay buffer (50 mM HEPES pH 7.0, 25 mM $KHCO_3$, 1.5 mM $(NH_4)_2SO_3$, 5 mM $MgCl_2$, 50 mM KCl, 1 mM TCEP, 1 mM NADH, 2.5 mM PEP, 40 U/mL PK/LDH and 0.2 mM NAG unless otherwise stated) alone or with varying concentrations of inhibitor for 20 min. The reaction was initiated by the addition of ATP to the assay mixture in a 384-well plate (Corning Cat# 3764) with a final volume of 15 μL. The reaction was monitored continuously at 340 nm for 60 min with a Tecan M1000 plate reader at room temperature. The linear portion of the progress curve was used for all kinetic fitting.

ADP-Glo® Assay

CPS1 activity was measured in an endpoint assay using the ADP-Glo® kit from Promega (Cat# V9102) to measure ADP formation. 50 nM CPS1 was incubated alone or with varying amounts of inhibitor in assay buffer (50 mM HEPES pH 7.0, 12.5 mM $KHCO_3$, 1.5 mM $(NH_4)_2SO_3$, 5 mM $MgCl_2$, 50 mM KCl, 1 mM TCEP, 0.01% TritonX 100, 0.0025% BSA and 0.2 mM NAG unless otherwise stated) for 20 min. The reaction was initiated with varying amounts of ATP in a 384-well plate (Corning Cat# 3820) with a final volume of 6 μL. After 60 min at room temperature, the reaction was terminated with 3 μL ADP-Glo reagent and allowed to sit at room temperature for 30 min. 3 μL of kinase detection reagent was then added and after 30 min luminescence was measured using an Envision plate reader.

Transcreener ADP2 FP® Assay

ADP formation from CPS1 was measured in an endpoint assay using the Transcreener ADP2 FP® kit from Bellbrook Labs (Cat # 3010-1K). 10 nM CPS1 was incubated with varying amount of inhibitor in assay buffer (50 mM HEPES pH 7.0, 12.5 mM $KHCO_3$, 1.5 mM $(NH_4)_2SO_3$, 5 mM $MgCl_2$, 50 mM KCl, 1 mM TCEP, 0.01% TritonX 100, 0.0025% BSA and 0.2 mM NAG unless otherwise stated) for 20 min. The reaction was initiated with varying amounts of ATP in a 384-well plate (Corning Cat# 3820) with a final volume of 6 μL. After 60 min the reaction was quenched with 6 uL of 30 mM EDTA. ADP Alexa Fluor 633 and detection antibody were added at a final concentration of 2 nM and 6 μg/mL, respectively. Fluorescence polarization was measured 30 min later on a Tecan M1000 plate reader.

Carbamoyl Phosphate Detection Assay

Carbamoyl phosphate produced by CPS1 was measured in an absorption assay as described previously (Levine and Kretchmer, 1971; Pierson, 1980). 250 nM CPS1 was incubated with varying amounts of compound in assay buffer (50 mM HEPES pH 7.0, 12.5 mM $KHCO_3$, 0.75 mM $(NH_4)_2SO_3$, 5 mM $MgCl_2$, 50 mM KCl, 1 mM TCEP, 0.01% TritonX 100, 0.0025% BSA, 0.2 mM NAG) for 20 min. The reaction was initiated with 5 mM ATP and allowed to proceed for 1 hr in a final assay volume of 20 μL in a 1.5 mL tube. The reaction was stopped with 1 μL 2 M hydroxylamine, then heated at 95°C for 10 minutes. 80 μL of a one to one mixture of solutions A and B (see below) was then added to each tube and mixture heated at 95°C for 15 min. Absorbance (458 nm) was then read on a Tecan M1000 plate reader after the solution was cooled to room temperature. Solution A was made

by dissolving 85 mg of antipyrine in 10 mL 40% H_2SO_4. Solution B was made by dissolving 62.5 mg diacetyl monoximine in 10 mL 5% acetic acid.

Carboxy Phosphate Synthesis (ATP A) Activity Assay

Carboxy phosphate synthesis at the carbamate synthetase domain (ATP A) was measured as a function of ADP formation in the absence of ammonia in the PK/LDH coupled assay. 100 nM CPS1 was incubated in the presence or absence of inhibitor in assay buffer (50 mM HEPES pH 7.0, 12.5 mM $KHCO_3$, 5 mM $MgCl_2$, 50 mM KCl, 1 mM TCEP, 0.01% TritonX 100, 0.0025% BSA, 1 mM NADH, 2.5mM PEP, 40 U/mL PK/LDH and 0.2 mM NAG) for 20 min. The reaction was initiated by the addition of ATP to the assay mixture in a 384-well plate (Corning Cat# 3764) with a final volume of 15 μL. The reaction was monitored continuously at 340 nm for 60 min with a Tecan M1000 plate reader at room temperature. The linear portion of the progress curve was used for all kinetic fitting.

Carbamate/ATP Synthesis (ATP B) Activity Assay

Enzymatic activity at the carbamoyl phosphate synthetase domain was measured in the reverse direction utilizing carbamoyl phosphate as the phosphate donor for ATP synthesis. 100 nM CPS1 was incubated in assay buffer (50 mM HEPES pH 7.0, 5 mM $MgCl_2$, 50 mM KCl, 1 mM TCEP, 0.01% TritonX 100, 0.0025% BSA and 0.2 mM NAG) with or without inhibitor for 20 min. The reaction was initiated with the addition of carbamoyl phosphate and ADP at a final concentration of 2 mM and 100 μM, respectively. The final volume was 6 μL in a 384-well plate (Corning Cat# 3820). After a 60 min incubation at room temperature, the reaction was terminated with 6 μL of Kinase-Glo® reagent (Promega, Kinase-Glo Max Cat# V6072). Luminescence was then measured using an Envision plate reader.

Activity at the carbamoyl phosphate synthetase domain was also measured using a continuous absorbance assay, utilizing a hexokinase/glucose 6-phosphate dehydrogenase enzyme coupled assay. 100 nM CPS1 was incubated in assay buffer (50 mM HEPES pH 7.0, 5 mM $MgCl_2$, 50 mM KCl, 1 mM TCEP, 0.01% TritonX 100, 0.0025% BSA, 1 mM NADPH, 100 U/mL hexokinase/glucose 6-phosphate dehydrogenase and varying NAG) before the addition of carbamoyl phosphate and ADP to initiate the reaction at a final concentration of 2 mM and 100 uM, respectively. The reaction volume was 15 μL. The reaction was monitored continuously at 340 nm at room temperature in a 384-well plate (Corning Cat# 3764) on a Tecan M1000 plate reader.

Equations

Steady-state kinetic data were fit globally to the following equations:

Mixed inhibition

$$v = V_{max}[S]/([S](1 + [I]/\alpha K_i) + K_m(1 + [I]/K_i))$$

Competitive inhibition

$$v = V_{max}[S]/([S] + K_m(1 + [I]/K_i))$$

CAD (CPS2) Activity Assay

CPS2 activity of CAD was measured as a function of ATP hydrolysis with the ADP-Glo® assay kit from Promega (Cat# V9102). 60 nM CAD was incubated with or without CPS1 inhibitor in assay buffer (50 mM HEPES pH 7.0, 50 mM $KHCO_3$, 2 mM Gln, 2 mM PRPP, 5 mM Asp, 10 mM $MgCl_2$, 50 mM KCl, 1 mM TCEP, 0.01% TritonX 100 and 0.0025% BSA) for 20 min. The reaction was initiated with 100 μM ATP at a final volume of 6 μL in a 384-well plate (Corning Cat# 3820). After 60 min at room temperature, the reaction was terminated with 3 μL ADP-Glo® reagent and allowed to sit at room temperature for 30 min. 3 μL of kinase detection reagent was then added and after 30 min luminescence was measured using an Envision plate reader.

Differential Scanning Fluorimetery (DSF)

Compound binding to CPS1 was confirmed in a DSF assay (Vedadi et al., 2006). 3 μM CPS1 was incubated with varying concentrations of compound in assay buffer (50 mM HEPES pH 7.0, 1 mM TCEP, and 0.005% Triton X 100) for 30 min in a 5 μL volume. 5 μL of a 2X concentration of protein thermal shift dye (Applied Biosystems, Cat# 4461) was added to CPS1. CPS1 melting temperature was then measured over a temperature gradient on a quantitative real-time PCR instrument (ViiA 7, Applied Biosystems).

Ligand Detection NMR Experiments

Sample preparation: All NMR samples were prepared in a final buffer containing 50 mM HEPES-d_{18} pH 7.0, 25 mM $KHCO_3$, 1.5 mM $(NH_4)_2SO_3$, 50 mM KCl, 5 mM $MgCl_2$, 1 mM TCEP-d_{16}, 5% glycerol-d_8, 10% D_2O, and 3.6% DMSO-d_6. Samples containing H3B-120 were prepared from a DMSO-d_6 stock solution at 4.2 mM and diluted with buffer or protein solution to reach a concentration of 150 μM. Prior to preparing sample containing CPS1, the protein was buffer exchanged on a Zeba™ Spin Desalting Column, 7K MWCO (Thermo scientific) and diluted in buffer to reach a final concentration of 5 μM. The final protein sample was then supplemented with 200 μM of N-acetyl glutamate.

All NMR experiments were acquired at 298 K on a 600 MHz Bruker Avance III Spectrometer equipped with a helium HFCN cryoprobe. The following NMR experiments were acquired: The 1D ^{1}H used for differential line broadening (DLB) employed the standard Bruker 1D ^{1}H sequence with excitation sculpting (zgesgp). Spectra were acquired with 64 scans. The T2-CPMG experiment employed is a modified version of the standard Bruker 1D ^{1}H experiment with excitation sculpting (zgesgp) with the addition of a CPMG pulse train after the initial 90-deg excitation pulse. The total duration of each spin echo was fixed to 1 msec (τ=500 μsec) whereas the number of echoes in the pulse train was varied according to the total time (T), ranging from 0 to 800 ms. The number of scans for all spectra was 16. The sequence employed for saturation transfer difference (STD) is a modified version of standard zgesgp; with water suppression using excitation sculpting with gradients with saturation applied at 0 and 20 ppm for the ON and OFF-resonance experiments, respectively.

Crystallization and Structure Determination

The CPS1-H3B-193 complex was crystallized in apo conditions as previously described (de Cima et al., 2015). Purified CPS1 protein was buffer exchanged into 50 mM glycyl-glycine pH 7.4, 50 mM KCl, 5% glycerol by several rounds of centrifugal filtration. CPS1 was concentrated to a 10 mg/ml final concentration then H3B-193 was added to a 5x excess molar ratio along with 1 mM AMPPNP and 1 mM NAG. Ligand bound complex was incubated for 1 hr at room temperature prior to setting up crystal drops. Ligand bound complex crystal grew by hanging drop vapor diffusion in 20% PEG 3350 and 0.2 M trisodium citrate after a week at 20°C. Crystallization buffer supplemented with 20% glycerol was used for cryoprotection. X-ray diffraction data were obtained at beamline GM/CA 23ID-D at Argonne National Laboratory. Data were processed with DIALS (Table S1). The structure was determined by molecular replacement with Phaser using the previously published apo structure (PDB code 5DOT) as a search model. Two molecules of CPS1 were found in the asymmetric unit. The initial difference map showed clear unambiguous additional density corresponding to the ligand. Initial automated building and refinement was done with Arp/WARP. Refmac5 and Coot were used for the final rounds of model building and refinement manually adjusting sidechains as necessary to fit in the density and provide optimal H-bond interactions for Asn/Gln/His where the orientation would otherwise be ambiguous. The final global statistics converged at R = 17.2% and Rfree = 20.9% and the structure overall has excellent geometry (summarized in Table S1). The position of the modeled ligand was validated at the end of the refinement with a final calculated omit map (Figure S3B). The coordinates were deposited in the PDB with accession code 6UEL.

Hepatocyte Urea Production Assay

Pooled primary human hepatocytes were purchased from BioIVT and cultured according to BioIVT standard protocols in Invitrogro CP media. Cells were thawed and plated on 96-well collagen coated plates with 50,000 cells/well. After hepatocytes attached to the collagen coated plate, plating media was removed and replaced with fresh media containing DMSO or CPS1 inhibitor. After 16 hrs the media was removed from cells and assayed for urea using a urea detection kit from Bioassay Systems (Cat # DIUR-100). Briefly, 50 μL of media was mixed with 200 μL of detection reaction and allowed to develop for 30 min at room temperature prior to reading absorbance at 520 nm on a Tecan M1000 plate reader.

MetID

An aliquot of 500 μL cell lysing solvent (45% methanol + 45% acetonitrile +10% water with 0.1% formic acid and 0.1 μg/mL Labetolol) was added to a 1.5 mL tube which contained a cell pellet from 1 well of a 6-well dish of treated hepatocytes. The tube was vortexed for one minute and placed in liquid nitrogen in a thermal cup. The tube was put through three cycles of freeze and thaw, then vortexed and centrifuged at 13,000 rpm for 5 minutes. The supernatant was transferred to a new centrifuge tube, and then the pellet was rinsed with another aliquot of 500 μL water with 0.1% formic acid, vortexed and centrifuged. The supernatant was combined, and 200 μL supernatant was transferred to 96-well plate and brought to dryness under a stream of nitrogen. The sample was then reconstituted in 100 μL of water with 0.1% formic acid.

LCMS analyses on each sample was performed using a Waters Q-TOF G2-XS interfaced with an Acquity UPLC system (Waters, Milford, MA, USA). An Phenomenex Luna Phenomenex PFP column, 3.0 x 100 mm was used for chromatographic separation. The mobile phases consisted of A: H2O/0.1% formic acid and B: acetonitrile/0.1% formic acid. The LC gradient was as follows: 0 - 6 min 2 - 4% B, 1 - 5 min 4 - 30% B, 5 - 6.5 min 30 - 60% B, 6.5 - 7 min 60 - 95% B, 7 - 7.5 min 95 - 95% B, 7.5 - 8 min 95 - 2% B, 8 - 10 min 2 - 2% B at a flow rate of 750 mL/min. For MS detection, uracil, adenosine and guanosine were analyzed using positive ionization mode, while TMP, UMP and uridine were carried out in negative mode. Waters Quanlynx^{TM} software was used to process the high resolution full scan MS data using a 20 milliDalton extraction window.

QUANTIFICATION AND STATISTICAL ANALYSIS

All of the statistical analysis and statistical details of experiments can be found in the Figure Legends section. GraphPad Prism was used to produce Figures 1D, 2A–2D, 3A, 5B, 6A–6D, S2A, S2C, S3A, S5C, and S5D.

For Figures 1D, 2A–2D, 3A, 5B, S2A, and S5D, data are represented as mean +/- SD of independent technical replicates (n=2, n represents the number of wells tested in a 384-well plate).

For Figures 6B and 6C, data are represented as mean +/- SD of independent biological replicates (n=3, n represents the number of wells tested in a 6-well plate).

For Figures 6A, S2C, S3A, and S5C, data are represented as a single data point (n =1, n represents the number of wells tested in a 384-well plate).

For Figure 6D, data are represented as the mean +/- SD of independent biological replicates (n=4, n represents the number of wells from a 6-well plate).

DATA AND CODE AVAILABILITY

The PDB code for CPS1 bound to H3B-193 reported in this study is 6UEL.